Univerzita Komenského v Bratislave

Fakulta matematiky, fyziky a informatiky

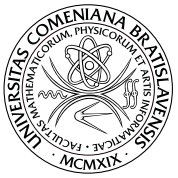

Mgr. Juraj Smieško

Autoreferát dizertačnej práce

Intrinsic Charm in Proton

na získanie akademického titulu philosophiae doctor
v odbore doktorandského štúdia:

4.1.5. Jadrová a subjadrová fyzika

Miesto a dátum:

Bratislava
2019

Dizertačná práca bola vypracovaná v dennej forme doktorandského štúdia na Katedre jadrovej fyziky a biofyziky Fakulty matematiky, fyziky a informatiky Univerzity Komenského v Bratislave.

Predkladateľ: Mgr. Juraj Smieško
Fakulta matematiky, fyziky a informatiky
Univerzity Komenského v Bratislave
Katedra jadrovej fyziky a biofyziky
Mlynská dolina F1
842 48 Bratislava

Školiteľ: prof. RNDr. Stanislav Tokár, CSc.
Fakulta matematiky, fyziky a informatiky
Univerzity Komenského v Bratislave
Katedra jadrovej fyziky a biofyziky
Mlynská dolina F1
842 48 Bratislava

Študijný odbor: 4.1.5. Jadrová a subjadrová fyzika

Študijný program: Jadrová a subjadrová fyzika

Predseda odborovej komisie:
prof. RNDr. Jozef Masarik, DrSc.
Fakulta matematiky, fyziky a informatiky
Univerzity Komenského v Bratislave
Katedra jadrovej fyziky a biofyziky
Mlynská dolina F1
842 48 Bratislava

Introduction

This year, 2019, marks the 55th anniversary of quarks, the particles which make up not only protons, but all of hadrons. This is largely known thanks to three men M. Gell-Mann [1, 2], G. Zweig [3] and R. Feynman [4]. By merging and extending their ideas [5–8] in the 60s and 70s it is now imagined, that the proton consists of three valence quarks (bearing most of the proton mass) and gluon and quark sea. Another quark antiquark pairs can appear at any time in this quark and gluon sea as a result of gluon conversion and they are called the sea quarks. The quarks come in six flavors: up (u) and down (d) quarks could be both valence and from the sea, while the others, strange (s), charm (c), bottom (b) and top (t) could come only from the sea.

The idea of a non-zero *intrinsic* (valence like) heavy quark (c and b) component of the proton originates in the 80s. It was proposed by S. J. Brodsky and coauthors to explain the abundant production of D^+ and Λ_c^+ in the forward region of the phase space. They considered the existence of a five quark state $|uudc\bar{c}\rangle$ in the proton [9, 10]. There were also other models, for example one considered quasi-two-body state $\bar{D}^0(uc)\bar{\Lambda}_c^+(udc)$ in the proton [11].

First, experiments at Hadron-Electron Ring Accelerator (HERA) have found, that the probability to find the intrinsic charm (IC) in the proton (the weight of the relevant Fock state in the proton) has to be less then 3.5% [11–14]. For the b quark, the probability to find intrinsic bottom (IB) is suppressed by a factor of $m_c^2/m_b^2 \approx 0.1$, where m_c and m_b are masses of c and b quarks, respectively. This comes from vacuum polarization mechanism [15].

Later, studies of prompt photon and $c\,(b)$-jet production in $p\bar{p}$ collisions at center-of-mass energy $\sqrt{s} = 1.96$ TeV at the Tevatron [16–19] observed that the ratio of the experimental transverse momentum p_T^γ spectrum of the prompt photons accompanied by the c-jets to relevant theoretical expectation (based on conventional parton distribution function (PDF)) increases up to a factor of about 3 when p_T^γ reaches 110 GeV. Predictions of prompt photon and c-jet production with IC probability of 3.5% in different pseudorapidity regions for the Large Hadron Collider (LHC) were done in Ref. [20].

The LHC with pp collisions at $\sqrt{s} = 8$ or 13 TeV offers new kinematical regions for study of the PDFs. Although, almost all pp processes at LHC energies could be sensitive to the charm PDF, the semi-inclusive production of $c\,(b)$-jet accompanied by photons or Z bosons is considered to be the most sensitive to the intrinsic heavy quark (IQ) contributions [20].

1 Theoretical basis

1.1 Extrinsic and Intrinsic Quark

The PDF $f_a(x, \mu)$ is defined as the probability density for finding parton a (quark q or gluon g) carrying a certain momentum fraction x at resolution scale μ. Because of the inherent non-perturbative nature of partons which cannot be observed as free particles, parton den-

sities can not be fully obtained by perturbative quantum chromodynamics (pQCD) for low values of scale μ bellow μ_0. Above this scale μ_0, the PDF can be calculated by solving the glspqcd evolution equations Dokshitzer-Gribov-Lipatov-Altarelli-Parisi (DGLAP) [21–23]. The unknown input for the evolution of the glspdf is usually obtained by fitting observables to experimental data.

The nucleon is usually regarded as a three quark bound state, however its actual Fock state structure (in quantum chromodynamics (QCD)) has to be much more complicated. If one defines the proton state at the infinite momentum frame (at equal time on the light cone) then the proton has a general decomposition in terms of color singlet eigenstates of the free Hamiltonian, i. e. $|uud\rangle, |uudg\rangle, |uudq\bar{q}\rangle, \ldots$ [10]. Since hadrons are color singlets, all infra-red divergences cancel and each of the amplitudes $\langle p|uud\rangle$, etc., has a well defined probability. Although proton states such as $|uudc\bar{c}\rangle$ and $|uudb\bar{b}\rangle$ are rare, the existence of hidden charm and other heavy quarks within the proton bound state may lead to new phenomena.

It is important to distinguish two types of contributions to the hadron quark and gluon distributions: *extrinsic* and *intrinsic*. Extrinsic (or ordinary) quarks and gluons are generated on a short time scale in association with a large transverse momentum reactions. Their distribution functions satisfy standard QCD evolution equations. The intrinsic quarks and gluons exist over a time-scale independent of any probe momentum, and are associated with the bound state (zero-momentum transfer regime) hadron dynamics and are believed to be of non-perturbative origin. [10].

Property which differentiates an IQ state such as $|uudQ\bar{Q}\rangle$ from extrinsic states is that the heavy constituents tend to carry the largest fraction of the momentum of the hadron: $\langle x_{\mathrm{Q}}\rangle > \langle x_{\mathrm{q}}\rangle$. Here x_{Q} is momentum fraction of the heavy quark, and x_{q} is momentum fraction of the light quark.

The probability distribution for the 5-quark state ($|uudc\bar{c}\rangle$) within the light-cone dynamics in the Brodsky-Hoyer-Peterson-Sakai (BHPS) model can be after few approximations written as [9, 11, 24]:

$$P(x) = 600wx^2\Big[6x(1+x)\ln x + (1-x)(1+10x+x^2)\Big], \tag{1}$$

where w is the probability to find the Fock state $|uudc\bar{c}\rangle$ in the proton.

Contribution of IC into overall probability to find charm quark in the proton is illustrated in Fig. 1. The figure shows several charm density distributions as a function of x at $\mu^2 = 10$ GeV^2 and $\mu^2 = 10^4$ GeV^2 from CTEQ66c PDF set [14]. The dotted line shows standard perturbative sea charm density distribution and other lines show the charm density distribution with various values of IC contribution w. One can see from the enhancement at $x \sim 0.2 - 0.5$, that the distribution with IC contribution is more than order of magnitude larger.

Since gluons and sea quarks play the key role in hard processes of open charm hadroproduction, it is expectable to see some excess of heavy quarks originating from IC over the

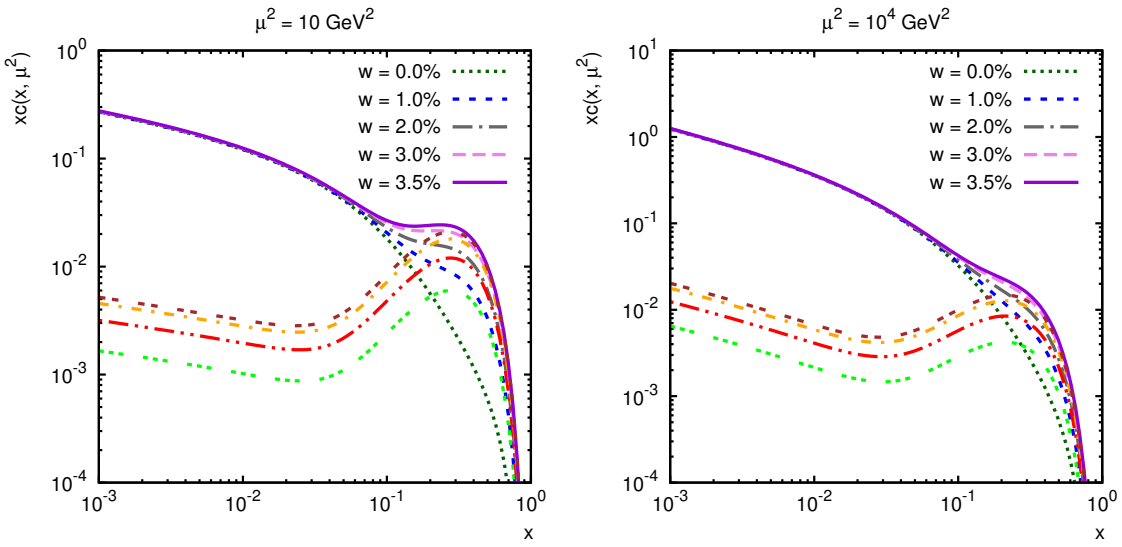

Figure 1: The total charmed quark density $xc(x,\mu^2)$ as a function of x at different values of w at $\mu^2 = 10$ GeV^2 (left) and $\mu^2 = 10^4$ GeV^2 (right). The dotted line corresponds to no IC contribution ($w = 0\%$) and continuous line corresponds to maximal non contradictory IC contribution ($w = 3.5\%$). Between the triple dotted line and double dashed lines, the only IC part of the $xc(x,\mu^2)$ is shown [25].

sea quarks at $x > 0.1$. Therefore the existence of this intrinsic charm component can lead to some enhancement in the inclusive spectra of open charm hadrons, produced at large pseudorapidities η and large transverse momenta p_{T} [26].

1.2 Intrinsic charm in hard pp collisions

According to the model of hard scattering [27–32], the relativistic invariant inclusive spectrum of the hardprocess $p+p \to h+X$ can be related to the elastic parton-parton subprocess $i+j \to i'+j'$, where i and j are the partons (quarks and gluons), by the formula [29, 30, 33]:

$$E\frac{\mathrm{d}\sigma}{\mathrm{d}^3\mathbf{p}} = \sum_{i,j}\int \mathrm{d}^2\mathbf{k}_{\mathrm{T}i}\int \mathrm{d}^2\mathbf{k}_{\mathrm{T}j}\int\limits_{x_i^{\min}}^{1}\mathrm{d}x_i\int\limits_{x_j^{\min}}^{1}\mathrm{d}x_j f_i(x_i,\mathbf{k}_{\mathrm{T}i})f_j(x_j,\mathbf{k}_{\mathrm{T}j})\frac{\mathrm{d}\sigma_{ij}(\hat{s},\hat{t})}{\mathrm{d}\hat{t}}\frac{D^{\mathrm{h}}_{i,j}(z_{\mathrm{h}})}{\pi z_{\mathrm{h}}}. \quad (2)$$

Here $\mathbf{k}_{i,j}$ and $\mathbf{k}'_{i,j}$ are the four-momenta of the partons i or j before and after the elastic parton parton scattering, respectively; $\mathbf{k}_{\mathrm{T}i}$, $\mathbf{k}_{\mathrm{T}j}$ are the transverse momenta of the partons i and j; z is the fraction of the hadron momentum from the parton momentum; $f_{i,j}$ is the PDF; and $D_{i,j}$ is the fragmentation function (FF) of the parton i or j into a hadron h.

When the transverse momenta of the partons are neglected in comparison with the longitudinal momenta, the variables $\hat{s}$, $\hat{t}$, $\hat{u}$ and z_{h} can be presented in the following forms [34]:

$$\hat{s} = x_i x_j s, \qquad \hat{t} = x_i\frac{t}{z_{\mathrm{h}}}, \qquad \hat{u} = x_j\frac{u}{z_{\mathrm{h}}}, \qquad z_{\mathrm{h}} = \frac{x_1}{x_i}+\frac{x_2}{x_j}, \quad (3)$$

where

$$x_1 = -\frac{u}{s} = \frac{x_T}{2}\cot\frac{\theta}{2}, \qquad x_2 = -\frac{t}{s} = \frac{x_T}{2}\tan\frac{\theta}{2}, \qquad x_T = 2\frac{\sqrt{tu}}{s} = 2\frac{p_T}{\sqrt{s}}. \tag{4}$$

Here as usual, $s = (\mathbf{p}_1 + \mathbf{p}_2)^2$, $t = (\mathbf{p}_1 - \mathbf{p}_1')^2$, $u = (\mathbf{p}_2 - \mathbf{p}_1')^2$, and $\mathbf{p}_1$, $\mathbf{p}_2$, $\mathbf{p}_1'$ are the 4-momenta of the colliding protons and the produced hadron h, respectively; θ is the scattering angle for the hadron h in the pp center-of-mass system. The lower limits of the integration in Eq. 2 are

$$x_i^{\min} = \frac{x_T \cot\dfrac{\theta}{2}}{2 - x_T \tan\dfrac{\theta}{2}}, \qquad x_j^{\min} = \frac{x_i x_T \tan\dfrac{\theta}{2}}{2x_i - x_T \cot\dfrac{\theta}{2}}. \tag{5}$$

Actually, the parton distribution functions $f_i(x_i, \mathbf{k}_{Ti})$ also depend on the four-momentum transfer squared Q^2 that is related to the Mandelstam variables $\hat{s}$, $\hat{t}$, $\hat{u}$ for the elastic parton parton scattering [30, 34]

$$Q^2 = \frac{2\hat{s}\hat{t}\hat{u}}{\hat{s}^2 + \hat{t}^2 + \hat{u}^2} \tag{6}$$

One can see that the Feynman variable x_F of the produced hadron, can be expressed via the variables p_T and η, or θ (the hadron scattering angle) in the pp center-of-mass system,

$$x_F \equiv \frac{2p_z}{\sqrt{s}} = \frac{2p_T}{\sqrt{s}}\frac{1}{\tan\theta} = \frac{2p_T}{\sqrt{s}}\sinh\eta. \tag{7}$$

At small scattering angles of the produced hadron this formula becomes

$$x_F \sim \frac{2p_T}{\sqrt{s}}\frac{1}{\theta}. \tag{8}$$

It is clear that for fixed p_T an outgoing hadron must possess small θ or large η in order to have large x_F (to follow forward, or backward direction).

In the fragmentation region (of large x_F) the Feynman variable x_F of the produced hadron is related to the variable x of the IC quark in the proton, and according to the longitudinal momentum conservation law, the $x_F \simeq x$ (and $x_F < x$). Therefore, there could be visible excess in the inclusive spectrum of, for example, K mesons due to the enhancement of the intrinsic strangness (IS) distribution at $x > 0.1$.

The lower limits of the integration in Eq. 2 can be also presented in the following form:

$$x_i^{\min} = \frac{x_R + x_F}{2 - (x_R - x_F)}, \qquad x_j^{\min} = \frac{x_i(x_R - x_F)}{2x_i - (x_R + x_F)}, \tag{9}$$

where $x_R = 2p/\sqrt{s}$. One can see from Eq. 9 that, at least, one of the low limits $x_i^{\min}$ of the integral Eq. 2 must be greater or equal to x_F. Thus if $x_F \geq 0.1$, then $x_i^{\min} > 0.1$, where the ordinary (extrinsic) charm distribution is completely negligible in comparison with the IC distribution. Therefore, at $x_F \geq 0.1$, or equivalently at the charm momentum fraction

$x_c > 0.1$ the IC distribution intensifies the charm PDF contribution into charm hadroproduction substantially (see Fig. 1). As a result, the spectrum of the open charm hadroproduction can be increased in a certain region of p_T and η (which corresponds to $x_F \geq 0.1$ in accordance to Eq. 9). It should be emphasized that this excess (or even the possibility to observe relevant events in this region) is due to the non-zero contribution of IC component at $x_c > x_F > 0.1$, here the extrinsic (sea generated) component completely vanishes.

1.3 Prompt photons and c-jet production

Apart from searching for IC contribution in proton using inclusive open charm hadroproduction in pp collisions, one can search for it in a production of real prompt photon γ accompanied by a c-jet. An advantage of prompt photons lays in their point like electromagnetic coupling to the proton constituents. The main contribution to the reaction $pp \to \gamma + c + X$ within leading order (LO) QCD is given by hard subprocess presented in Fig. 2.

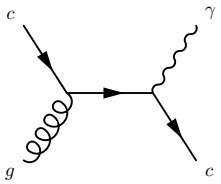

Figure 2: The LO Feynmann diagram for the hard process $c + g \to \gamma + c$.

Other LO contributing subprocesses are $gg \to c\bar{c}, qc \to qc, gc \to gc$ with bremsstrahlung $c(\bar{c}) \to c(\bar{c})\gamma$. Contribution of those processes is sizable at low p_T^γ and can be neglected at $p_T^\gamma > 60$ GeV according to [35]. At next-to-leading order (NLO) of QCD it is the higher order correction, $gc \to gc\gamma$, to the Compton subprocess that dominates the cross section.

According to Eq. 7 one can see that, for certain values of the photon transverse momentum p_T^γ and pseudorapidity η^γ, the momentum fraction of the photon x_F can be higher than 0.1, therefore the fraction of the initial charm quark must also be above 0.1, where the IC contribution in the proton is enhanced. Therefore, one can expect some non-zero IC signal in the E_T^γ spectrum of the reaction $pp \to \gamma + c + X$ [20].

The prediction of the transverse momentum differential cross-section of prompt photon p_T^γ accompanied by a c-jet is presented in Ref. [20], see Fig. 3. This prediction is calculated at NLO in the massless quark approximation with the following cuts applied: $p_T^\gamma > 45$ GeV, $p_T^c > 20$ GeV and rapidity of the jet in the interval $|y^\gamma| \leq 2.37$. Presented figure shows a forward rapidity region ($1.52 \leq |y^\gamma| < 2.37$) and in the upper half the solid blue line represents the differential cross section calculated with the radiatively generated charm PDF (CTEQ66), the dash-dotted green line uses as input the sea-like PDF (CTEQ66c4) and the dashed red line the BHPS PDF (CTEQ66c2 — with IC contribution 3.5%). In the lower half of the figure the above distributions are divided by the distribution acquired using the

CTEQ66 PDF. The shaded yellow region, represents the scale dependence. The scale is varied within $\mu/2$ and 2μ.

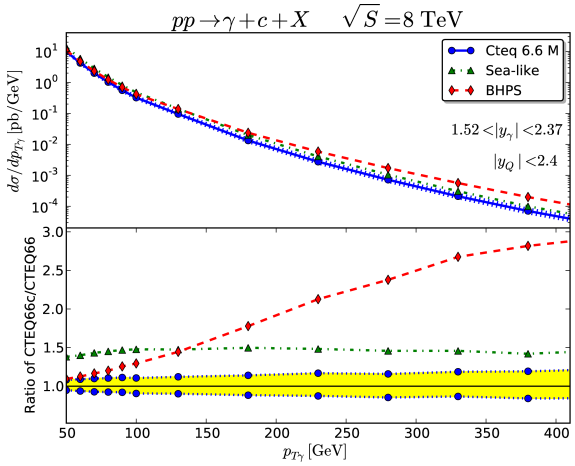

Figure 3: The $\mathrm{d}\sigma/\mathrm{d}p_{\mathrm{T}}^{\gamma}$ distribution versus the transverse momentum of the photon for the process $pp \to \gamma + c + X$ at $\sqrt{s} = 8$ TeV using CTEQ6.6M (solid blue line), BHPS CTEQ6c2 (dashed red line) and sea-like CTEQ6c4 (dash-dotted green line), for forward photon rapidity $1.52 < |y_\gamma| < 2.37$ and the ratio of these spectra with respect to the CTEQ6.6M (solid blue line) distributions. The calculation was done within the NLO QCD approximation [20].

2 Tile-in-One

2.1 Tile Calorimeter Software

To support basic Tile Calorimeter (TileCal) data monitoring and maintenance activities several tools were developed during commissioning and maintained by different groups. However, these tools made use of distinctive technologies and/or data sources that require different forms of data recovery. Also the documentation for any particular tool was not well consolidated. Most of these tools were developed independently, without following the same guidelines, sometimes lacking basic software infrastructure and implemented without a global perspective of the calorimeter. Therefore, in many cases, they overlap in the objectives and resources with each other. Besides, in order to perform a single task, the collaborator must navigate through different tools, databases and software, which is time consuming and susceptible to mistakes.

Thus, the use, maintenance and enhancement of existing functionalities becomes time consuming and costly work. Tile-in-One (TiO) aims to integrate different Tile tools, sharing the same infrastructure and accessing common services, such as: access to different databases, user authentication, commonly used libraries, and software infrastructure to allow collaborators to integrate their own tools.

2.2 Tile-in-One Platform

The idea of Tile-in-One (TiO) is, even after several unsuccessful attempts, deemed to be valuable for the TileCal community, that is why the project is being rebooted. This time, however, it will function just as a simple bridge or gatekeeper between the client and small web applications called plugins. The job of a plugin will be to make all the steps necessary for creating response to the client request. The diagram of the platform can be seen in Fig. 4 and the properties of the system are described in following points:

- The main server is just a bridge (reverse proxy), its purpose is to provide authentication and authorization for the plugins behind it.
- A plugin is a small independent web application.
- Due to requirements on different data sources and avoiding interface between plugins every plugin is enclosed in its own Virtual Machine (VM).
- Plugins are based on one of the three templates, since the plugin developers mainly will not be skilled in web development.
- All the source code for the plugin will be stored in a Git repository. CERN runs it's instance of GitLab server, which is centrally managed.
- There will be a person or a group responsible for the maintenance of the plugin.
- Platform developers will have full access to all the VMs in order to be able to take over the maintaining of the machine.

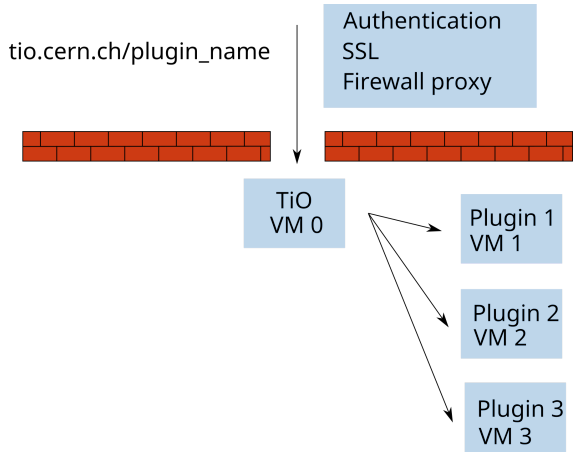

Figure 4: The diagram of the new Tile-in-One platform.

Plugin development requires from the plugin developer to design, program and operate the whole machine with a web server on top. It is expected that the majority of the plugin developers will not be sufficiently skilled in web development, therefore the platform will provide setup scripts to setup a VM and three plugin templates for the web application. The platform will provide the following templates:

- Simple Static Plugin Template:
  - Dynamic elements only on the user side (JavaScript).
  - Server could regularly run cron jobs to update data files (e.g. csv or json).
  - Ideal for simple status pages of a subsystem.
  - Implemented with HTML, CSS, JavaScript.
- Simple Dynamic Plugin Template:
  - All the above functionality.
  - Can process parameters on the server site.
  - Ideal for simple plugins with several parameters.
  - Implemented with Python and Bottle.
- Complex Dynamic Plugin Template:
  - All the above functionality.
  - Can store web page data in database.
  - Ideal for complex plugins, which require user management.
  - Implemented with Python and Django.

The new implementation of TiO platform will rely on several open source projects as well as services already used at CERN and was designed to use as much existing software and services as possible. In the future, the tasks related to the creation and development of plugins will be transferred into CERN-GitLab's CI/CD environment. Since the CERN computing rules does not allow for accessing unfinished plugins outside CERN network two main servers are in the operation. First one, called production server, serves the finished plugins to all authenticated clients. The second one, called development server, serves unfinished plugins only to authenticated clients inside CERN network.

In conclusion, new common web space for the TileCal related offline data quality tools was created. After realizing that manpower resources would not be sufficient in keeping the current platform afloat decision was made to design a much lighter and more stable platform with emphasis on using already developed and common software. There is hope, that this will lead to an easier transfer of knowledge about inner workings of the platform, quicker and easier development of the plugins, and also easier integration of the currently working TileCal web tools into the TiO platform.

3 Simulated Samples

In the investigation of possible IC in proton employing the A Toroidal LHC ApparatuS (ATLAS) semi-inclusive $pp \to \gamma + c$-jet measurement [36] two approaches to create simulated samples with variable IC contribution w were employed.

3.1 Sherpa NLO Sample

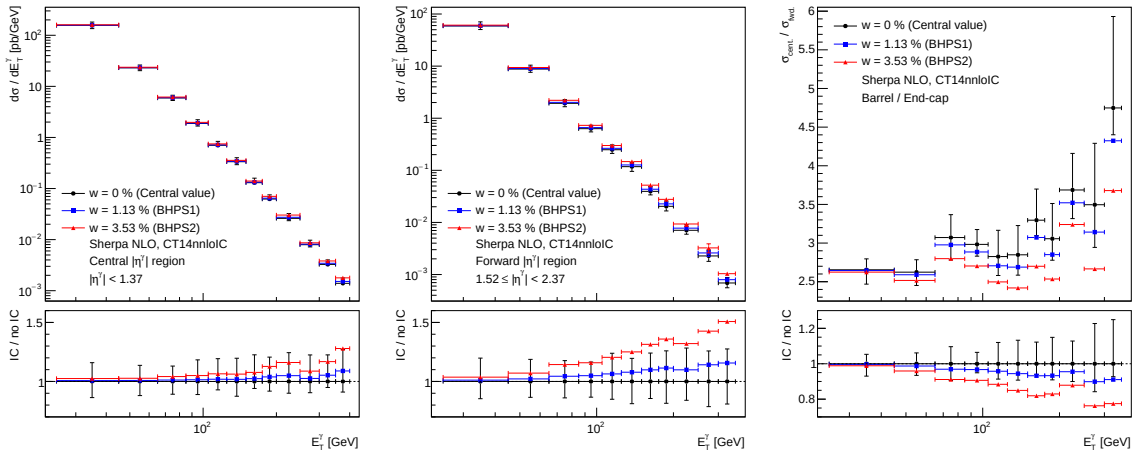

Figure 5: The SHERPA NLO simulated E_{T}^{γ} spectra of $pp \to \gamma + c$-jet process and the relative uncertainties of these spectra in two pseudorapidity $|\eta^{\gamma}|$ regions central (left), forward (middle) and their ratio (Barrel/End-cap, right) at various values of IC probability w.

3.1.1 Event Generation

The Monte Carlo generator SHERPA [37–40] (version 2.2.4) with NLO, i.e. $O(\alpha\alpha_s^2)$, matrix elements generated by OPENLOOPS [41–43] (version 1.3.1) within ME+PS@NLO model is employed to generate sample of γ + jet + up to 3 additional jets at $\sqrt{s} = 8$ TeV. The heavy flavor quarks in the calculation were considered massless. The calculation employs several PDF sets with the help of LHAPDF6 [44], main PDF set is CT14nnlo [45], which is extended by CT14nnloIC [46] set. The CT14nnloIC set is an IC addition to the CT14nnlo set and contains only central value and several IC values in two models BHPS and SEA [46]. Two BHPS sets were used designated BHPS1 and BHPS2, which contain IC with $w = 1.13\%$ and $w = 3.53\%$ respectively. Additionally NNPDF 3.0 [47], CT10nlo [48] and CTEQ66 [14] PDFs were used to assess effects of different PDFs on simulated E_{T}^{γ} spectra of $\gamma + c$-jet production.

The sample is generated in five E_{T}^{γ} slices with boundaries of 25, 45, 85, 150, 300 and 450 GeV, which were chosen to match the bin boundaries of the ATLAS $pp \to \gamma + c$-jet measurement. The size of the whole generated sample is about 1 million events. Additional sample for $\sqrt{s} = 13$ TeV predictions is about 0.8 million events.

3.1.2 Event selection

For the event selection the custom Rivet [49] analysis is used, which was later validated against the Rivet analysis of the ATLAS $pp \to \gamma + c$ measurement [50].

The analysis starts with the search for leading photon with $E_{\mathrm{T}}^{\gamma} > 25$ GeV and $|\eta^{\gamma}| < 2.37$, events with leading photon falling into the ATLAS Calorimeter gap $1.37 < |\eta^{\gamma}| < 1.56$ being discarded. The selected leading photons are required to satisfy sliding calorimeter

isolation criterion $E_{\mathrm{T}}^{\mathrm{iso}} < 4.8\ \mathrm{GeV} + 0.0042 \times E_{\mathrm{T}}^{\gamma}$. The $E_{\mathrm{T}}^{\mathrm{iso}}$ variable is calculated as a sum of transverse energy of all particles with a lifetime greater than 10 ps with a separation in angle of $\Delta R < 0.4$ around the photon. Muons and neutrinos are excluded because they deposit little or no energy in the calorimeter. Also, the $E_{\mathrm{T}}^{\mathrm{iso}}$ variable is corrected for the energy density of the underlying event [51].

The jets are built using the anti-k_t algorithm, which takes as input all particles in the event with a lifetime greater than 10 ps and radius parameter of $R = 0.4$. Only jets with $p_{\mathrm{jet}}^{\gamma}$ greater than 20 GeV and separation from the leading photon $\Delta R > 0.4$ are considered. The selected leading jet must satisfy $|\eta^{\mathrm{jet}}| < 2.5$ requirement, otherwise the event is discarded. In addition, the leading photon and leading jet separation criteria are applied, discarding all events where $\Delta R < 1.0$ between the two. If a b hadron with $p_{\mathrm{T}} > 5$ GeV is found to be in a cone of $R = 0.3$ around the leading jet, it will be considered to be a b-jet and the event is discarded. In contrary, if a c hadron with $p_{\mathrm{T}} > 5$ GeV is found to be in a cone of $\Delta R = 0.3$ around the leading jet, it will be considered to be a c-jet and the event is kept.

3.1.3 Uncertainties

Four types of systematic uncertainties are considered in the Sherpa NLO sample. The scale uncertainty, which is assessed by multiplying or dividing the renormalization μ_{R} and factorization μ_{F} scales by a factor of two, both separately and simultaneously. The final uncertainty is taken as an envelope of the deviations from the nominal prediction. The uncertainty of the CT14nnlo PDF set is assessed by varying spectra using all 56 eigenvectors provided and the largest deviation, out of the all possible, with respect to the nominal value is taken as the final PDF uncertainty. The uncertainty in the strong coupling α_{s} value is assessed by changing its value to 0.117 and 0.119. The uncertainty coming from the uncertainty of the total fiducial cross section calculation is taken into account by varying the normalization of the E_{T}^{γ} spectra by one standard deviation of the Sherpa NLO total cross section calculation.

3.2 Combined QCD Sample

The Combined QCD approach combines two techniques to analytically calculate E_{T}^{γ} spectra of $pp \to \gamma + c$-jet process in the kinematic regime, where they are most suitable [52]. First the k_{T}-factorization formalism is employed to calculate the leading contributions from the $O(\alpha\alpha_{\mathrm{s}}^2)$ off-shell gluon gluon fusion $g^*g^* \to \gamma c\bar{c}$. In this way one takes into account the conventional perturbative charm contribution to associated γc production. In addition there are backgrounds from jet fragmentation.[1]

The IC contribution is computed using the $O(\alpha\alpha_{\mathrm{s}})$ QCD Compton scattering $cg^* \to \gamma c$ amplitude, where the gluons are kept off-shell and incoming quarks are treated as on-shell

[1] Here α is the electromagnetic coupling constant and α_{s} is the QCD coupling constant.

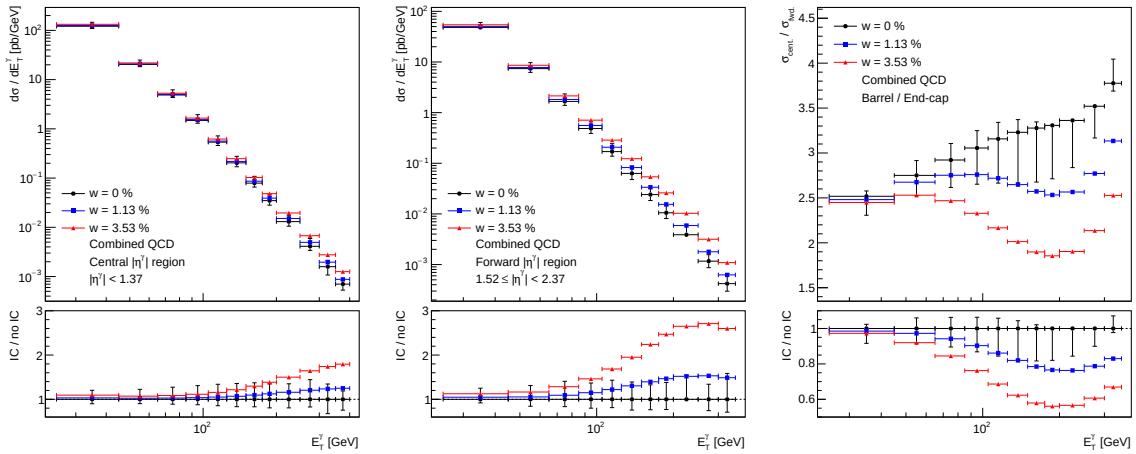

Figure 6: The Combined QCD simulated E_{T}^{γ} spectra of $pp \to \gamma + c$-jet process and the relative uncertainties of these spectra in two pseudorapidity $|\eta^{\gamma}|$ regions central (left), forward (middle) and their ratio (Barrel/End-cap, right) at various values of IC probability w.

partons. This is justified by the fact that the IC contribution begins to be visible at the domain of large $x \geq 0.1$, where its transverse momentum can be safely neglected.

The k_{T}-factorization approach has technical advantages, since one can include higher-order radiative corrections using the transverse momentum dependent (TMD) parton distribution of the proton [53]. Technically, the numerical solution of the Ciafaloni-Catani-Fiorani-Marchesini (CCFM) gluon evolution equation [54, 55] is employed [56], which resumes the leading logarithmic terms, proportional to $\log 1/x$, up to all orders of perturbation theory.

In addition, several standard pQCD subprocesses involving quarks in the initial state are taken into account. These are the flavor excitation $cq \to \gamma cq$, quark antiquark annihilation $q\bar{q} \to \gamma c\bar{c}$ and quark gluon scattering subprocess $qg \to \gamma qc\bar{c}$. These processes become important at large transverse momenta E_{T}^{γ} or at large parton longitudinal momentum fraction x, which is the kinematics needed to produce high E_{T}^{γ} events; it is the domain where the quarks are less suppressed or can even dominate over the gluon density. The calculation relays on the conventional (DGLAP) factorization scheme, which should be reliable in the large x region.

In the calculation, the relatively old PDF is used, CTEQ66c [14]. It is due to technical requirement on PDF to be k_{T}-factorization compatible and at the same time to provide few distributions with non zero IC contribution.

The only systematic uncertainty of the calculation considered in this case is the uncertainty coming from the variation of factorization μ_{F} and renormalization μ_{R} scale. The scales are multiplied or divided by a factor of two and the extreme cases of deviation from the nominal prediction are taken as the final uncertainty.

4 Results

Employing the measurement of semi-inclusive $pp \to \gamma + c$-jet process at 8 TeV done by the ATLAS collaboration [36] and standalone SHERPA NLO and Combined QCD simulated samples, investigation of possible IC component of the proton PDF is conducted.

4.1 Simulated Samples versus the Measurement

The comparisons between ATLAS $\gamma + c$-jet measurement and simulated samples in different $|\eta^\gamma|$ ranges are presented in Fig 7. One can see that the SHERPA NLO sample is in agreement with the measurement in the central $|\eta^\gamma|$ region within the total uncertainties of the measurement. In case of the Combined QCD sample one can observe underestimation of the measurement at high E_{T}^γ. There is also slight overestimation of the measurement in the first bin of the E_{T}^γ spectra in the both samples, which can be attributed to large scale uncertainties coming from off-shell gluon gluon fusion. This subprocess dominates the E_{T}^γ region below 100 GeV. The underestimation of the E_{T}^γ spectra in the case of the Combined QCD sample at large E_{T}^γ can be explained by absence of the effects of parton showers, hadronization and loop NLO diagrams in this calculation.

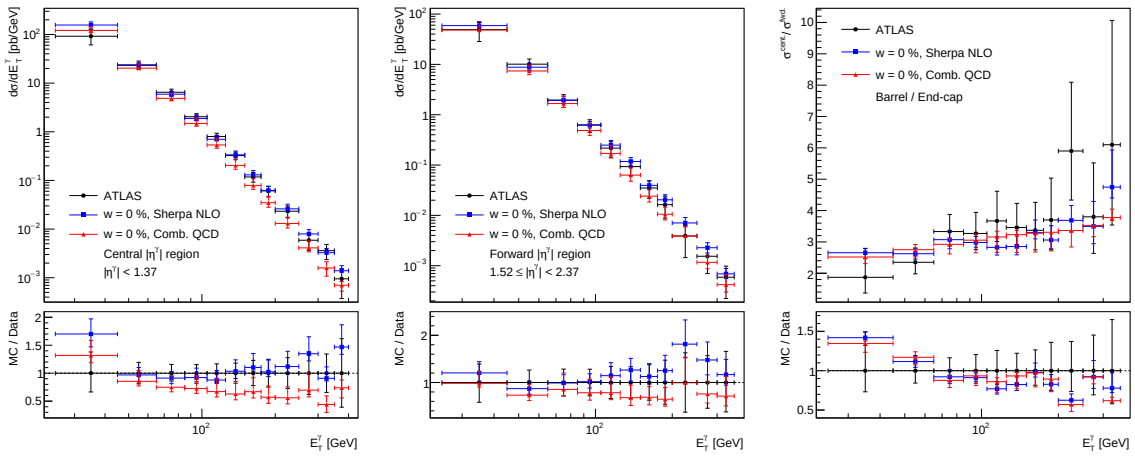

Figure 7: The ATLAS measured E_{T}^γ spectrum of $pp \to \gamma + c$-jet process [36] compared with the SHERPA NLO and the Combined QCD simulated samples in two $|\eta^\gamma|$ regions: central (left), forward (middle) and their ratio (Barrel/End-cap, right).

In case of the forward $|\eta^\gamma|$ region the situation is similar, but there is a smaller underestimation in the case of the Combined QCD sample at large E_{T}^γ. There is also a better agreement between the simulated samples and the measurement at small E_{T}^γ. The ratio of the two $|\eta^\gamma|$ regions (central $|\eta^\gamma|$ region to forward $|\eta^\gamma|$ region) exhibits good agreement between the simulated samples and the measurement.

4.2 Variable Intrinsic Charm

4.2.1 Sherpa NLO Sample

The recent versions of the SHERPA generator can for every event provide multiple additional weights [57] at NLO level, this means that one can obtain spectra with various values of α_s, various values of scales or various PDFs. Apart from using this feature for the determination of uncertainties of the simulated E_T^γ spectra, one can use it to vary the content of the intrinsic charm in it. Since all the other variables of the generated events are kept the same, one can interpolate between the event weights at fixed IC probability values coming from the PDF.

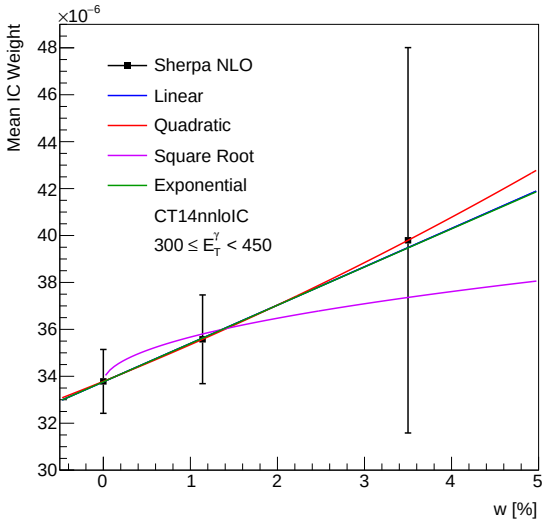

Figure 8: Mean of absolute IC SHERPA NLO event weight values at different fixed IC probability w fitted with several functions.

The SHERPA NLO sample uses combination of two PDFs: the CT14nnlo and its IC addition CT14nnloIC, using them three event IC weights in BHPS model are available Ω_0 (0% IC), Ω_1 designated as BHPS1, which corresponds to the IC probability $w = 1.13\%$ and Ω_2 designated as the BHPS2 ($w = 3.53\%$). In order to obtain the event IC weight at any IC probability w these weights are fitted with quadratic function, Eq. 10, on event by event basis.

$$\Omega = a_1 + a_2 w + a_3 w^2 \tag{10}$$

Here Ω is SHERPA event weight value for a given IC probability w and a_1, a_2 and a_3 are fit parameters. Several other functions were tested and the quadratic function gives smallest and most consistent χ^2 across all the events. In Fig. 8 the mean of absolute IC weight values at different fixed IC probability w is shown along with error bars, which show spread of the values. The weight values in the SHERPA NLO calculations are also negative, in this case the absolute value of the weights is taken to perform fit and resulting weight value is after

the fit multiplied by -1. Fig. 8 also illustrates small difference between most of the fitting functions.

4.2.2 Combined QCD Sample

In case of the Combined QCD, one has to find an interpolation between two charm densities at the scale μ^2 to obtain variable IC probability w in E_{T}^{γ} spectra of $\gamma + c$-jet production. Two- and three-point interpolation of the all parton (quark and gluon) distributions for $w_0 = 0\%$, $w_1 = 1\%$ and $w_2 = 3.5\%$ was performed, which corresponds to the CTEQ66 (central value), CTEQ66c BHPS1 and CTEQ66c2 BHPS2, respectively. Two interpolation functions were investigated: linear and quadratic. The difference between the linear and the quadratic interpolation functions in the interval $0 < w \leq 3.5\%$ is not greater than 0.5% [25], that is why, the quadratic interpolation was chosen. The quadratic interpolation was employed for the all parton flavors at μ_0 and $w < w_2$ to satisfy the quark and gluon sum rules, see [58, 59]. At $w = w_2$ the quark sum rule is satisfied automatically in the used PDF because the intrinsic light $q\bar{q}$ contributions are included [14].

4.3 Intrinsic Charm Fitting Method

The determination of the w value from the ATLAS $\gamma + c$-jet measurement started with validation of the simulated E_{T}^{γ} spectra against the measurement in the central $|\eta^{\gamma}|$ region, see Sec. 4.1. One can see, that the measurement is satisfactorily described in the central $|\eta^{\gamma}|$ region using the Sherpa NLO sample without IC. On the other hand, the Combined QCD sample description underestimates the measurement, but stays within the total uncertainties. Since the uncertainties of the measurement and also simulated samples are comparable in size with the possible IC signal only an upper limit could be determined instead of precise value of the IC probability.

To obtain the upper limit w_{ul} on possible IC contribution in proton, a simple method of employing simulated spectra (ratios) containing known values of IC probability w was employed. Using the methods described in Sec. 4.2 to obtain the variable IC, a set of 1500 template spectra (ratios) were generated with IC probability in range $0 \leq w < 7.5$ %. In case of the Sherpa NLO sample the quadratic fit was employed and in the case of the Combined QCD sample it was the quadratic interpolation. The templates were generated for the forward $|\eta^{\gamma}|$ region, where the inclusion of IC has the effect of increasing the spectrum at high E_{T}^{γ} and for the Barrel/End-cap ratio where the inclusion has the effect of decreasing the ratio. To compare a template and the measured spectra the χ^2 was calculated as follows.

$$\chi^2(w) = \sum_{i=1}^{n} \frac{\left[y_i - f(w)_i\right]^2}{\sigma_i^2} \tag{11}$$

Here y_i is the measurement, $f(w)_i$ is the simulated sample with known w value and σ_i is the sum in quadrature of the uncertainties coming from the measurement and the

uncertainties coming from the simulated sample. For all the templates the χ^2 is calculated creating a curve. The minimum of the χ^2 curve determines the central value w_{cent} and the upper limit w_{ul} is determined as the w value that corresponds to the minimum of χ^2_{min} plus one, since there is only one fit parameter.

The employment of this simple fitting method is justified by negligible correlation between the bins of the E_{T}^{γ} spectra in the both $|\eta^{\gamma}|$ regions and in the case of the Barrel/End-cap ratio also by negligible correlations between bins of the two $|\eta^{\gamma}|$ regions. For the reason of large correlations between the bins of $\gamma + c$-jet and $\gamma + b$-jet measurement the fit using their ratio was not realized.

4.4 Upper Limit on Intrinsic Charm in Proton

The resulting upper limit of the IC contribution in proton in the case of the Sherpa NLO sample is $w_{\text{ul}} = 1.97\%$ at 68% CL obtained from the E_{T}^{γ} spectrum of the $\gamma + c$-jet production measured in the forward $|\eta^{\gamma}|$ region. The simulated samples employed in the IC fitting method are too different in respect to each other, which prevented one to be used as a cross check for the other. However, resulting upper limit w_{ul} in the case of the Sherpa NLO sample is considered more reliable, since this sample better describes measured E_{T}^{γ} spectrum of the $\gamma + c$-jet production in the central $|\eta^{\gamma}|$, this is mainly because of inclusion of all NLO diagrams, parton showers and hadronization.

4.4.1 Sherpa NLO Sample

Upper limit on IC in proton determined with the help of the Sherpa NLO simulated sample is presented in Fig. 9 and Fig. 10. The Fig. 9 shows the E_{T}^{γ} spectra of $\gamma + c$-jet with the contribution from IC at the upper limit value $w_{\text{ul}} = 1.97\%$ at 68% CL in the central and forward $|\eta^{\gamma}|$ regions. The limit was obtained by fitting the full E_{T}^{γ} spectra of forward $|\eta^{\gamma}|$ region as described in Sec. 4.3. The left panel of Fig. 10 shows another way of obtaining the IC limit. In this case the IC upper limit is obtained from the Barrel/End-cap ratio and resulting value is $w_{\text{ul}} = 2.26\%$ at 68% CL. The limit obtained from employing the forward $|\eta^{\gamma}|$ region is considered more reliable due to its smaller sensitivity to the incompatibilities between the simulation and the measurement. In Fig. 10 (right) the χ^2 dependence on the IC percentage w for the both cases of upper limit determination is shown.

Fig. 10 shows a rather weak χ^2 sensitivity to the w value in the both IC upper limit determination cases, which is caused by large experimental and theoretical uncertainties. The χ^2 is slightly more sensitive to the w in the case of employing forward $|\eta^{\gamma}|$ region, this results in a smaller IC upper limit. The central value of the fit w_{cent} is in the both cases 0. Also in the both cases of upper limit determination the obtained values are relatively close, the result is around 2% at 68% CL.

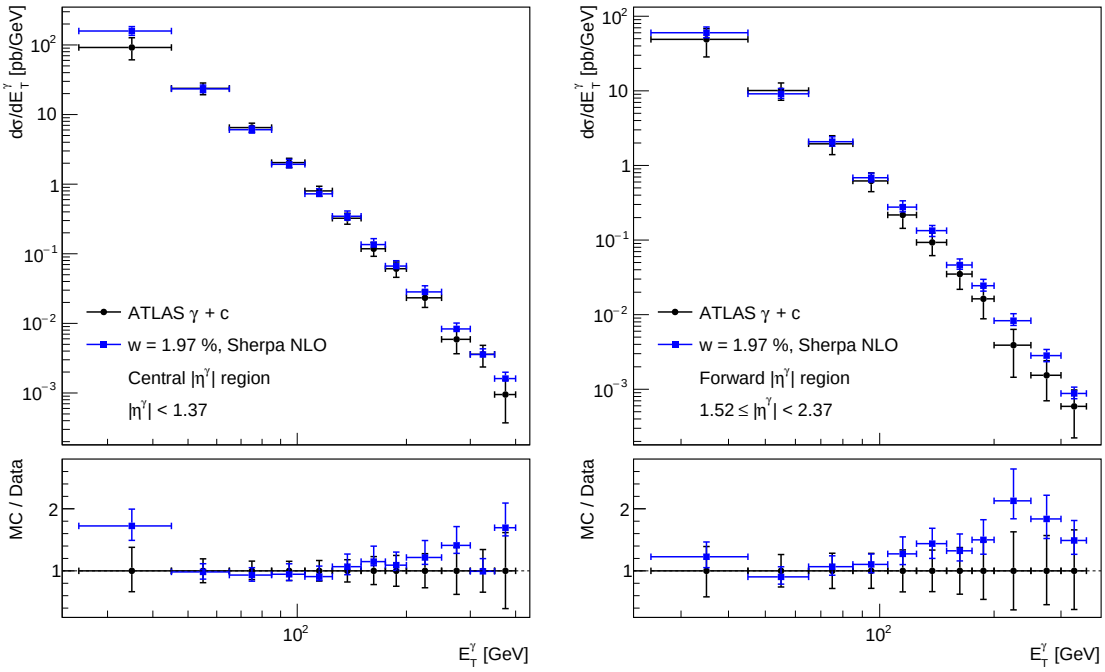

Figure 9: The E_{T}^{γ} spectrum of $\gamma + c$-jet from the SHERPA NLO sample compared with the ATLAS measurement in two $|\eta^{\gamma}|$ regions. Both panels show the simulated spectrum at the upper limit IC contribution $w_{\mathrm{ul}} = 1.97\%$ at 68% CL.

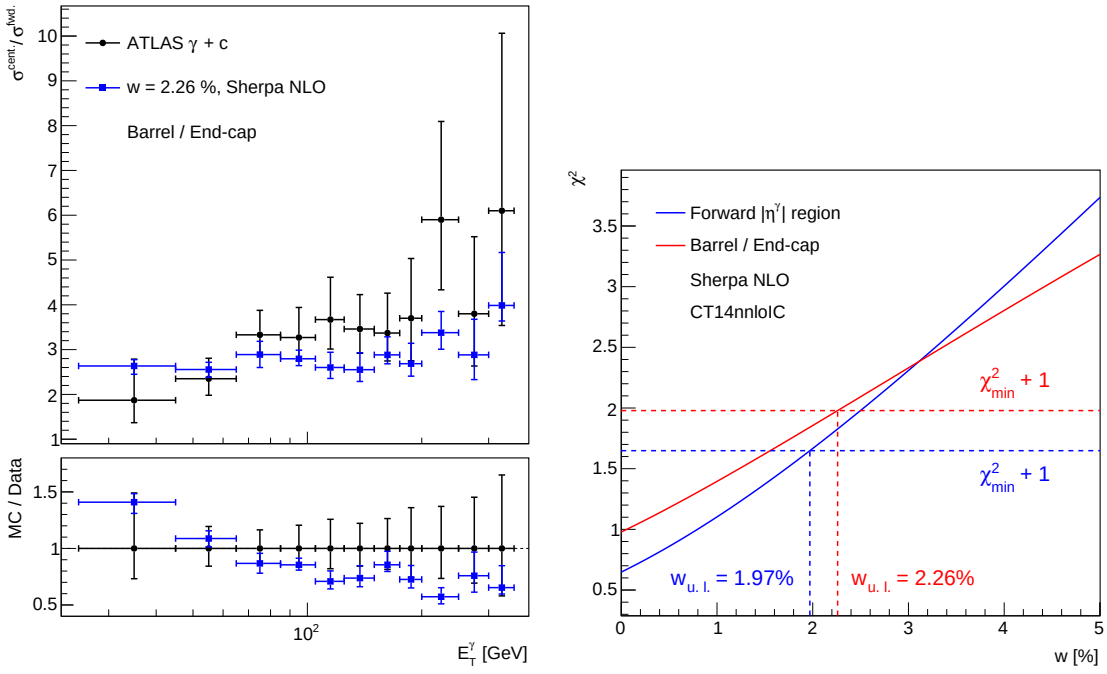

Figure 10: The ratio of the E_{T}^{γ} spectra in the central $|\eta^{\gamma}|$ region to the E_{T}^{γ} spectra in the forward $|\eta^{\gamma}|$ region (Barrel / End-cap ratio) of $\gamma + c$-jet process from the SHERPA NLO sample at the upper limit IC contribution $w_{\mathrm{ul}} = 2.26\%$ at 68% CL compared with the ATLAS measurement (left). The χ^2 as a function of w for two cases of upper limit determination based on the E_{T}^{γ} spectra in the forward $|\eta^{\gamma}|$ region and the Barrel/End-cap ratio (right).

4.4.2 Combined QCD Sample

The IC probability w fitting method was also repeated with the Combined QCD simulated sample and the E_{T}^{γ} spectra for both $|\eta^{\gamma}|$ rapidity regions compared to the ATLAS measurement are presented in Fig. 11. The E_{T}^{γ} spectra contain IC upper limit value $w_{\mathrm{ul}} = 2.91\%$ at 68% CL, which was determined by employing full E_{T}^{γ} spectra of forward $|\eta^{\gamma}|$ region as described in Sec. 4.3. In the left panel of Fig. 12 the upper limit of $w_{\mathrm{ul}} = 0.69\%$ at 68% CL obtained by employing the Barrel/End-cap ratio is shown. The figure also shows in the right panel the χ^2 dependence of both fitting options on the IC contribution w.

The upper limit obtained by employing the forward $|\eta^{\gamma}|$ region is not coinciding with the limit obtained by employing the Barrel/End-cap ratio. Also, the fits does not produce the same central value, for the forward $|\eta^{\gamma}|$ region fit it is $w_{\mathrm{cent}} = 1.06$ and for the Barrel/End-cap ratio it is $w_{\mathrm{cent}} = 0$. The χ^2 dependence on w in right panel of Fig. 12 shows much different shapes with the Barrel/End-cap ratio employing fit having a very sharp χ^2 dependency, resulting in the smallest upper limit w_{ul}. The source of this discrepancy can be attributed to an inability of the Combined QCD model to describe E_{T}^{γ} spectra of $\gamma + c$-jet production in forward $|\eta^{\gamma}|$ region well enough, see Fig. 7. This just resulted in filling up missing cross section with the IC contribution, especially at large E_{T}^{γ}. The Combined QCD model does not include parton showers and hadronization, which turns out to be crucial for the upper limit of IC determination from E_{T}^{γ} spectra of $\gamma + c$-jet production. Therefore, the results obtained by employing the SHERPA NLO simulated sample, which include these effects, are considered to be more reliable.

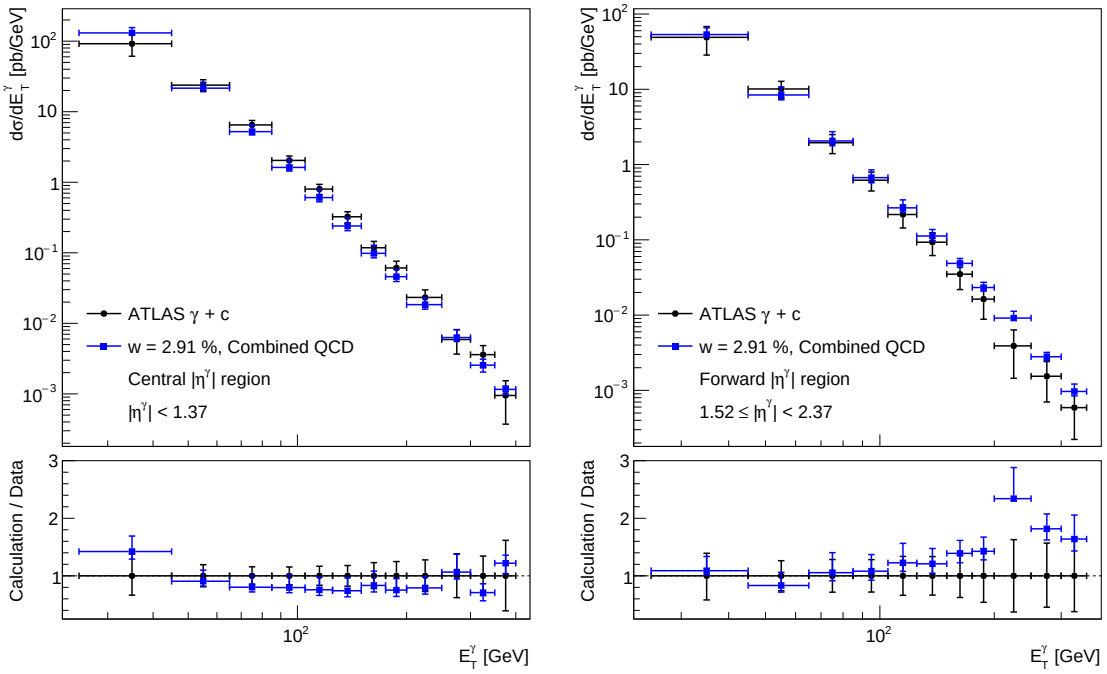

Figure 11: The E_{T}^{γ} spectrum of $\gamma + c$-jet from the Combined QCD sample compared with the ATLAS measurement in two $|\eta^{\gamma}|$ regions. Both panels show the simulated spectrum at the upper limit IC contribution $w_{\mathrm{ul}} = 2.91\%$ at 68% CL.

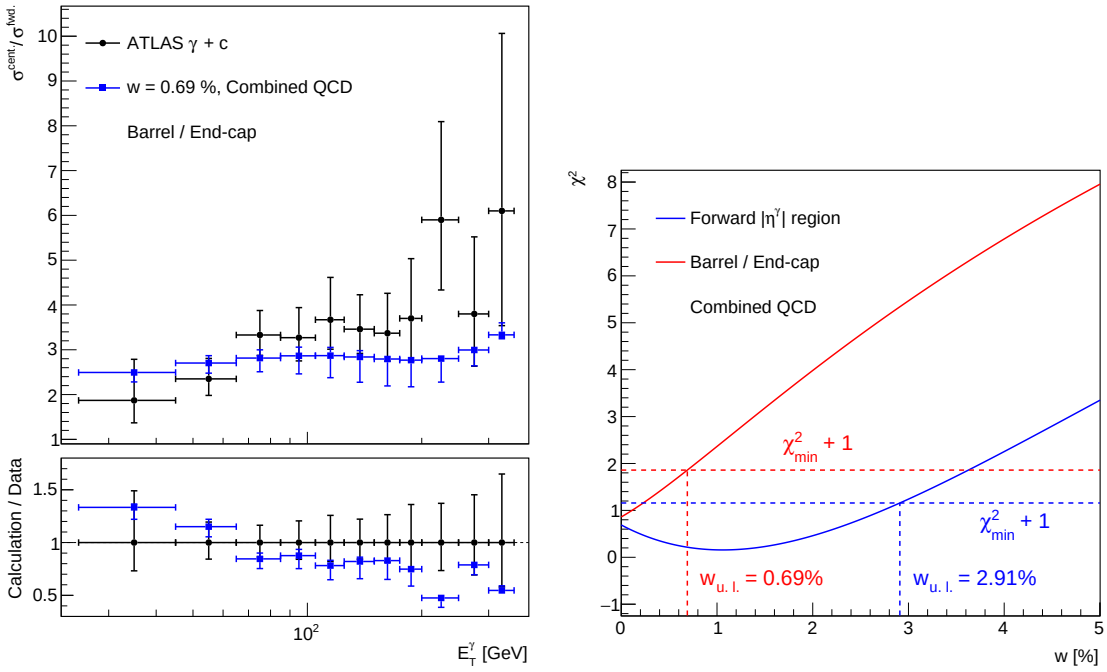

Figure 12: The ratio of the E_{T}^{γ} spectra in the central $|\eta^{\gamma}|$ region to the E_{T}^{γ} spectra in the forward $|\eta^{\gamma}|$ region (Barrel / End-cap ratio) of $\gamma + c$-jet process from the Combined QCD sample at the upper limit IC contribution $w_{\mathrm{ul}} = 0.69\%$ at 68% CL compared with the ATLAS measurement (left). The χ^2 as a function of w for two cases of upper limit determination based on the E_{T}^{γ} spectra in the forward $|\eta^{\gamma}|$ region and the Barrel/End-cap ratio (right).

4.5 Predictions for $\sqrt{s} = 13$ TeV Measurement

With the Run 2 of the LHC coming to an end, the final collected luminosity by the ATLAS experiment is around 140 fb^{-1}. This luminosity is more than enough to enable more precise measurement of $\gamma + c$-jet differential cross section in E_{T}^{γ}.

The effect of IC on the E_{T}^{γ} spectra of γ+c-jet at $\sqrt{s} = 13$ TeV is shown in Fig. 13. The figure shows a comparison of the IC effect at $\sqrt{s} = 8$ TeV versus $\sqrt{s} = 13$ TeV. One can see that in the case of $\sqrt{s} = 13$ TeV the IC effect is smaller, this is due to two reasons. First, the peak of the IC contribution will be shifted towards higher E_{T}^{γ}, this comes from the relationship Eq. 7 between E_{T}^{γ} and x_{F}. Second, it is suspected, that the contribution to the prompt photon spectra from diagrams which do not propagate IC grows quicker than from the ones which propagate it. The IC upper limit from a possible future $\sqrt{s} = 13$ TeV measurement could be improved only if a substantial reduction of systematic uncertainties of the measurement takes place.

4.6 Summary

A first estimate of the intrinsic charm probability in the proton has been carried out utilizing recent ATLAS measurement of the prompt photon production accompanied by the c-jet

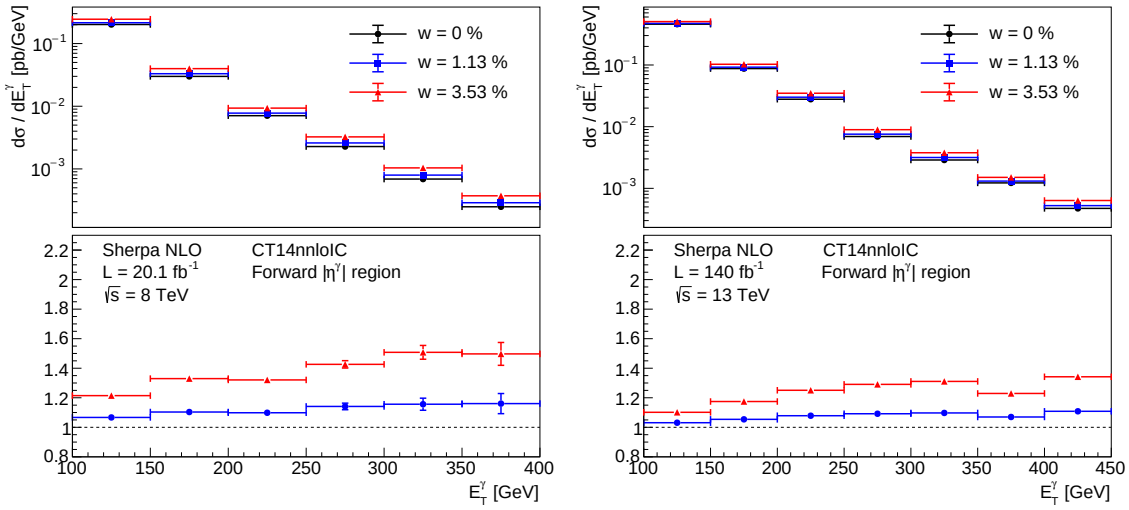

Figure 13: Differential cross sections in E_{T}^{γ} of the $\gamma+c$-jet production at two center-of-mass energies $\sqrt{s} = 8$ TeV (left) and $\sqrt{s} = 13$ TeV (right). The error bars show the statistical uncertainties only.

at $\sqrt{s} = 8$ TeV [36]. The estimated upper limit of the IC probability in the proton is 1.97% with 68% CL. The precision of this analysis is limited by the experimental systematic uncertainties — mainly, by the c tagging uncertainty which is predominantly connected with the light jet scaling factors. It is also limited by the theoretical QCD scale uncertainties. The PDF uncertainties are also considered, but they play only minor role together with the statistical uncertainties.

Contrary to the most recent estimations of NNPDF 3.1 $w = 0.16 \pm 0.14\%$ [60] or of H. Abdolmaleki and A. Khorramian $w = 0.94 \pm 0.20\%$ [61] only the upper limit of the IC probability w can be obtained from a single ATLAS $\gamma+c$-jet measurement [36]. If one desires to determine a possible IC contribution from a single measurement, the process $pp \to Z+c$ at high luminosity looks more promising, since $\gamma+c$-jet E_{T}^{γ} measurement is limited by large systematic uncertainties at high E_{T}^{γ}.

One can see that the IC upper limit is effectively insensitive to a change of the experimental statistical uncertainty. In order to obtain a more reliable information on the IC probability in proton from future LHC measurements at $\sqrt{s} = 13$ TeV it is needed to have a more realistic estimate of the theoretical scale uncertainties and to significantly reduce the systematic uncertainties, mainly the uncertainty connected with the c-jet tagging. This is needed for measurements of the cross sections of $\gamma+c$ and $\gamma+b$ production in pp-collisions at $\sqrt{s} = 13$ TeV especially at high transverse momentum with high statistics and for the ratio of the cross sections $\gamma + c$ and $\gamma + b$, which is expected to be more sensitive to the IC signal [25, 62]. Furthermore, measurements of the $Z/W+c/b$ production in pp collision at 13 TeV at high statistics could also provide a significant information on the IC contribution in proton [25, 62–64].

References

1. Gell-Mann, M. *CTSL-20, TID-12608* (1961).
2. Gell-Mann, M. *Phys. Lett.* **8**, 214–215 (1964).
3. Zweig, G. in *DEVELOPMENTS IN THE QUARK THEORY OF HADRONS. VOL. 1. 1964 - 1978* (eds Lichtenberg, D. & Rosen, S. P.) 22–101 (1964).
4. Feynman, R. P. *Phys. Rev. Lett.* **23**. [,494(1969)], 1415–1417 (1969).
5. Bjorken, J. D. & Glashow, S. L. *Phys. Lett.* **11**, 255–257 (1964).
6. Glashow, S. L., Iliopoulos, J. & Maiani, L. *Phys. Rev.* **D2**, 1285–1292 (1970).
7. Kobayashi, M. & Maskawa, T. *Prog. Theor. Phys.* **49**, 652–657 (1973).
8. Harari, H. *Phys. Lett.* **57B**, 265–269 (1975).
9. Brodsky, S. J., Hoyer, P., Peterson, C. & Sakai, N. *Phys. Lett.* **B93**, 451–455 (1980).
10. Brodsky, S. J., Peterson, C. & Sakai, N. *Phys. Rev.* **D23**, 2745 (1981).
11. Pumplin, J. *Phys. Rev.* **D73**, 114015. arXiv: hep-ph/0508184 [hep-ph] (2006).
12. Pumplin, J., Lai, H. L. & Tung, W. K. *Phys. Rev.* **D75**, 054029. arXiv: hep-ph/0701220 [hep-ph] (2007).
13. Peng, J.-C. & Chang, W.-C. *PoS* **QNP2012**, 012. arXiv: 1207.2193 [hep-ph] (2012).
14. Nadolsky, P. M. *et al. Phys. Rev.* **D78**, 013004. arXiv: 0802.0007 [hep-ph] (2008).
15. Polyakov, M. V., Schafer, A. & Teryaev, O. V. *Phys. Rev.* **D60**, 051502. arXiv: hep-ph/9812393 [hep-ph] (1999).
16. Abazov, V. M. *et al. Phys. Rev. Lett.* **102**, 192002. arXiv: 0901.0739 [hep-ex] (2009).
17. Abazov, V. M. *et al. Phys. Lett.* **B719**, 354–361. arXiv: 1210.5033 [hep-ex] (2013).
18. Abazov, V. M. *et al. Phys. Lett.* **B714**, 32–39. arXiv: 1203.5865 [hep-ex] (2012).
19. Aaltonen, T. *et al. Phys. Rev.* **D81**, 052006. arXiv: 0912.3453 [hep-ex] (2010).
20. Bednyakov, V. A., Demichev, M. A., Lykasov, G. I., Stavreva, T. & Stockton, M. *Phys. Lett.* **B728**, 602–606. arXiv: 1305.3548 [hep-ph] (2014).
21. Gribov, V. N. & Lipatov, L. N. *Sov. J. Nucl. Phys.* **15**. [Yad. Fiz.15,781(1972)], 438–450 (1972).
22. Altarelli, G. & Parisi, G. *Nucl. Phys.* **B126**, 298 (1977).
23. Dokshitzer, Y. L. *Sov. Phys. JETP* **46**. [Zh. Eksp. Teor. Fiz.73,1216(1977)], 641–653 (1977).
24. Blümlein, J. *Phys. Lett.* **B753**, 619–621. arXiv: 1511.00229 [hep-ph] (2016).
25. Lipatov, A. V., Lykasov, G. I., Stepanenko, Yu. Yu. & Bednyakov, V. A. *Phys. Rev.* **D94**, 053011. arXiv: 1606.04882 [hep-ph] (2016).

26. Lykasov, G. I., Bednyakov, V. A., Pikelner, A. F. & Zimine, N. I. *Europhys. Lett.* **99**, 21002. arXiv: 1205.1131 [hep-ph] (2012).
27. Efremov, A. V. *Yad. Fiz.* **19**, 196–202 (1974).
28. Nason, P., Dawson, S. & Ellis, R. K. *Nucl. Phys.* **B327**. [Erratum: Nucl. Phys.B335,260(1990)], 49–92 (1989).
29. Field, R. D. & Feynman, R. P. *Phys. Rev.* **D15**, 2590–2616 (1977).
30. Feynman, R. P., Field, R. D. & Fox, G. C. *Phys. Rev.* **D18**, 3320 (1978).
31. Mangano, M. L. *Phys. Usp.* **53**. [Usp. Fiz. Nauk180,113(2010)], 109–132 (2010).
32. Albino, S., Kniehl, B. A. & Kramer, G. *Nucl. Phys.* **B803**, 42–104. arXiv: 0803.2768 [hep-ph] (2008).
33. Bednyakov, V. A., Grinyuk, A. A., Lykasov, G. I. & Poghosyan, M. *Int. J. Mod. Phys.* **A27**, 1250042. arXiv: 1104.0532 [hep-ph] (2012).
34. Collins, J. C., Soper, D. E. & Sterman, G. F. *Adv. Ser. Direct. High Energy Phys.* **5**, 1–91. arXiv: hep-ph/0409313 [hep-ph] (1989).
35. Lipatov, A. V., Malyshev, M. A. & Zotov, N. P. *JHEP* **05**, 104. arXiv: 1204.3828 [hep-ph] (2012).
36. Aaboud, M. *et al. Phys. Lett.* **B776**, 295–317. arXiv: 1710.09560 [hep-ex] (2018).
37. Gleisberg, T. *et al. JHEP* **02**, 007. arXiv: 0811.4622 [hep-ph] (2009).
38. Schumann, S. & Krauss, F. *JHEP* **03**, 038. arXiv: 0709.1027 [hep-ph] (2008).
39. Krauss, F., Kuhn, R. & Soff, G. *JHEP* **02**, 044. arXiv: hep-ph/0109036 [hep-ph] (2002).
40. Gleisberg, T. & Hoeche, S. *JHEP* **12**, 039. arXiv: 0808.3674 [hep-ph] (2008).
41. Cascioli, F., Maierhofer, P. & Pozzorini, S. *Phys. Rev. Lett.* **108**, 111601. arXiv: 1111.5206 [hep-ph] (2012).
42. Ossola, G., Papadopoulos, C. G. & Pittau, R. *JHEP* **03**, 042. arXiv: 0711.3596 [hep-ph] (2008).
43. Van Hameren, A. *Comput. Phys. Commun.* **182**, 2427–2438. arXiv: 1007.4716 [hep-ph] (2011).
44. Buckley, A. *et al. Eur. Phys. J.* **C75**, 132. arXiv: 1412.7420 [hep-ph] (2015).
45. Dulat, S. *et al. Phys. Rev.* **D93**, 033006. arXiv: 1506.07443 [hep-ph] (2016).
46. Hou, T.-J. *et al. JHEP* **02**, 059. arXiv: 1707.00657 [hep-ph] (2018).
47. Ball, R. D. *et al. JHEP* **04**, 040. arXiv: 1410.8849 [hep-ph] (2015).
48. Lai, H.-L. *et al. Phys. Rev.* **D82**, 074024. arXiv: 1007.2241 [hep-ph] (2010).
49. Buckley, A. *et al. Comput. Phys. Commun.* **184**, 2803–2819. arXiv: 1003.0694 [hep-ph] (2013).

50. Prince, S. https://rivet.hepforge.org/analyses/ATLAS_2017_I1632756.html (2019).
51. Cacciari, M. & Salam, G. P. *Phys. Lett.* **B659**, 119–126. arXiv: 0707.1378 [hep-ph] (2008).
52. Baranov, S. P., Jung, H., Lipatov, A. V. & Malyshev, M. A. *Eur. Phys. J.* **C77**, 772. arXiv: 1708.07079 [hep-ph] (2017).
53. Andersson, B. *et al. Eur. Phys. J.* **C25**, 77–101. arXiv: hep-ph/0204115 [hep-ph] (2002).
54. Ciafaloni, M. *Nucl. Phys.* **B296**, 49–74 (1988).
55. Catani, S., Fiorani, F. & Marchesini, G. *Nucl. Phys.* **B336**, 18–85 (1990).
56. Catani, S., Ciafaloni, M. & Hautmann, F. *Nucl. Phys.* **B366**, 135–188 (1991).
57. Bothmann, E., Schönherr, M. & Schumann, S. *Eur. Phys. J.* **C76**, 590. arXiv: 1606.08753 [hep-ph] (2016).
58. Chang, W.-C. & Peng, J.-C. *Phys. Lett.* **B704**, 197–200. arXiv: 1105.2381 [hep-ph] (2011).
59. Chang, W.-C. & Peng, J.-C. *Prog. Part. Nucl. Phys.* **79**, 95–135. arXiv: 1406.1260 [hep-ph] (2014).
60. Ball, R. D. *et al. Eur. Phys. J.* **C77**, 663. arXiv: 1706.00428 [hep-ph] (2017).
61. Abdolmaleki, H. & Khorramian, A. *Phys. Rev.* **D99**, 116019. arXiv: 1903.02583 [hep-ph] (2019).
62. Brodsky, S. J., Bednyakov, V. A., Lykasov, G. I., Smiesko, J. & Tokar, S. *Prog. Part. Nucl. Phys.* **93**, 108. arXiv: 1612.01351 [hep-ph] (2017).
63. Beauchemin, P.-H., Bednyakov, V. A., Lykasov, G. I. & Stepanenko, Yu. Yu. *Phys. Rev.* **D92**, 034014. arXiv: 1410.2616 [hep-ph] (2015).
64. Lipatov, A. V., Lykasov, G. I., Malyshev, M. A., Prokhorov, A. A. & Turchikhin, S. M. *Phys. Rev.* **D97**, 114019. arXiv: 1802.05085 [hep-ph] (2018).

Publikácie autora

V. A. Bednyakov, S. J. Brodsky, A. V. Lipatov, G. I. Lykasov, M. A. Malyshev, J. Smiesko, S. Tokar; *Constraints on the intrinsic charm content of the proton from recent ATLAS data*; Eur. Phys. J. **C79**, 92 (2019).

S. J. Brodsky, V. A. Bednyakov, G. I. Lykasov, J. Smiesko, S. Tokar; *The Physics of Heavy Quark Distributions in Hadrons: Collider Tests*; Prog. Part. Nucl. Phys. **93**, 108 (2017).

J. Smiesko, S. Hyrych; *An integrated system for data quality and conditions assessment for the ATLAS Tile Calorimeter*; `https://cds.cern.ch/record/2648822`.